Applied Surface Science Advances 32 (2026) 100956

Contents lists available at ScienceDirect

Applied Surface Science Advances

journal homepage: www.sciencedirect.com/journal/applied-surface-science-advances

Full Length Article

# Entropy-engineered spinel oxide coatings to enhance oxidation resistance and electrical performance of solid oxide fuel cell interconnectors

Cheng-Ju Tsai [a,b], Hideyuki Murakami [c], Yoshiaki Toda [c], Fan-Yi Ouyang [b,d,e], Hyoung Seop Kim [f,g], An-Chou Yeh [a,b,e,*]

[a] Department of Materials Science and Engineering, National Tsing Hua University, 101, Sec. 2, Kuang-Fu Road, Hsinchu 300044, Taiwan R.O.C
[b] High Entropy Materials Center, National Tsing Hua University, 101, Sec. 2, Kuang-Fu Road, Hsinchu 300044, Taiwan R.O.C
[c] Research Center for Structural Materials, National Institute for Materials Science, 1-2-1 Sengen, Tsukuba 305-0047, Japan
[d] Department of Engineering and System Science, National Tsing Hua University, 101, Sec. 2, Kuang-Fu Road, Hsinchu, 300044, Taiwan R.O.C
[e] Institute of Space Engineering, National Tsing Hua University, 101, Sec. 2, Kuang-Fu Road, Hsinchu 300044, Taiwan R.O.C
[f] Center for Heterogenic Metal Additive Manufacturing, Pohang University of Science and Technology (POSTECH), Pohang, Republic of Korea
[g] Graduate Institute of Ferrous & Eco Materials Technology, Pohang University of Science and Technology, Pohang, Republic of Korea

ARTICLE INFO

*Keywords:*
Solid oxide fuel cell
High-entropy alloy
Spinel coating
Area specific resistance
Cr-evaporation

ABSTRACT

This study investigates spinel oxide coatings derived from medium- to high-entropy alloy systems for solid oxide fuel cell interconnect applications. Alloy coatings of Fe-Mn-Co, Fe-Mn-Co-Cu, and Fe-Mn-Co-Cu-Ni are deposited on SUS430 stainless steel substrates utilizing a magnetron sputtering system and subjected to isothermal oxidation at 650 °C. Microstructural and phase analyses reveal the anomalous formation of hematite layers and Cr-Fe mixed oxide structures in Fe-Mn-Co and Fe-Mn-Co-Cu coatings, which indicates greater Fe diffusion at the substrate/coating interface during the early stage of oxidation comparing to that of Fe-Mn-Co-Cu-Ni coating. Theoretical calculations confirm that the hematite and Cr-Fe oxides significantly increase the area specific resistance of Fe-Mn-Co and Fe-Mn-Co-Cu coated steels at 650 °C. Notably, the Fe-Mn-Co-Cu-Ni coating can exhibit superior electrical conductivity, and resistances to oxidation and Cr-evaporation. This study demonstrates that entropy-engineered composition can promote the formation of single phase spinel, enhance phase stability, and can potentially be beneficial for long-term performance of solid oxide fuel cell as coating material for interconnects.

## 1. Introduction

As global energy demand soars and environmental concerns grow, the pursuit of highly efficient renewable energy sources has become a primary objective of scientific research [1,2]. Solid Oxide Fuel Cells (SOFCs), like other fuel cells, directly convert chemical energy into electrical energy through electrochemical reactions [3–5]. However, SOFCs stand out due to their solid electrolyte, enabling high-temperature operation and power generation in several MWs [6]. These advantages make SOFCs a promising candidate for future energy systems. Recent advancements in SOFC technology have focused on developing electrolytes that enable intermediate operating temperatures (600–800 °C) [7,8]. Lower operating temperatures reduce the time and cost associated with heating and cooling the cell, while also enhancing overall performance [9]. Given these operating temperatures, cost-effective ferritic stainless steels, such as SUS430, SUS441, and Crofer 22, have become the predominant materials for interconnects or metal substrates of SOFC stacks [10].

However, Cr evaporation from stainless steel results in cathode Cr-poisoning, while long-term oxidation may cause oxide layer spallation [10–12]. These phenomena increase cell resistance, thereby reduce overall cell performance and durability. Over the past decade, spinel oxide coatings have been recognized as effective barriers against Cr diffusion, which exhibit low electrical resistivity and coefficient of thermal expansion (CTE) values compatible with those of ferritic stainless steels (11.5–14.0 $\times$ $10^{-6}$ $K^{-1}$) [13,14].

While most studies have concentrated on the performance of spinel coatings at around 800 °C [15–18], the properties of spinel coatings at

* Corresponding author at: Department of Materials Science and Engineering, National Tsing Hua University, 101, Sec. 2, Kuang-Fu Road, Hsinchu, 300044, Taiwan R.O.C.
*E-mail address:* yehac@mx.nthu.edu.tw (A.-C. Yeh).

https://doi.org/10.1016/j.apsadv.2026.100956
Received 26 October 2025; Received in revised form 31 January 2026; Accepted 17 February 2026
Available online 27 February 2026

lower operating temperatures, such as 650 °C, have been less studied. Operating at 650 °C enhances the long-term stability of SOFCs by reducing substrate degradation through slower oxidation and Cr evaporation [19,20]. However, the resulting oxide layer's microstructure and phase composition can differ significantly from those formed at higher temperatures. For instance, studies indicate the formation of Fe-rich spinel or $Fe_2O_3$ oxide layers in Co-based and Cu-based spinel coatings due to Fe diffusion from the substrate, which can persist for at least 3300 h at 650 °C and can negatively impact electrical performance [21,22]. Therefore, experimentally investigating spinel coating oxidation at 650 °C is crucial. Such studies can provide insights into the interdiffusion of coating elements, the types of oxide layers formed, and how their composition, structure, and thickness influence oxidation, Cr evaporation, and electrical resistance.

Inspired by the remarkable performance of high-entropy alloys, the concept of "high entropy" has recently been applied to oxides, e.g., (MgCoNiCuZn)O crystal, which is one of the first high-entropy oxides (HEOs) reported [23]. In general, HEO contains multiple metal cations filling in the cation sublattice sites with a random distribution. A key advantage of the "high entropy" design is the "sluggish diffusion effect", which is a phenomenon critical for SOFC application. The Cr-poisoning, oxidation behavior and diffusion of other elements are expected to be hindered in the HEO system. Zhao et al. prepared a 10-μm-thick Fe-Mn-Co-Cu-Ni multi-component spinel coating on SUS430 substrates using sputtering, which exhibited good thermal stability at 800 °C [24]. It is noteworthy that the multi-component spinel coating exhibited an excellent area specific resistance (ASR) value among other reported spinel coatings (e.g., Mn-Cu, Cu-Fe, Ni-Fe, and Fe-Co-Ni) prepared using the same method [25–28]. The superior conductivity of the multi-component spinel coating is attributed to enhanced polaron hopping at octahedral sites [29] and the absence of secondary oxide phases like NiO and CuO, which were present in Ni-Fe-based [27] and Cu-Fe-based [26] coatings, respectively. However, the specific contribution of each element to the thermal stability of the coating remains unclear. Additionally, a comprehensive understanding of the oxide layer composition and properties at 650 °C for the multi-component coatings is lacking. Further investigation is needed to elucidate these aspects through a systematic tuning of compositional complexity within multi-component systems.

The initial coating composition was inspired by the Cantor alloy, CoCrFeMnNi [30]. To mitigate the issue of Cr-evaporation, this work has replaced Cr with Cu, resulting in the five-element coating, Fe-Mn-Co-Cu-Ni. To eliminate the possibility of NiO formation, we then removed Ni to create the four-element Fe-Mn-Co-Cu coating. Finally, to prevent CuO formation, Cu was further removed, leaving a three-element coating of Fe-Mn-Co. In this study, three multi-component alloy coatings, designated as Coatings 1, 2, and 3, were deposited onto SUS430 substrates via magnetron sputtering using equimolar Fe-Mn-Co, Fe-Mn-Co-Cu, and Fe-Mn-Co-Cu-Ni targets, respectively. These coatings were subsequently oxidized to form spinel-based coatings during the oxidation test. The aim of this study is to investigate the oxidation resistance and the electrical performance of ternary to quinary multi-component oxide coatings at 650 °C. Additionally, the mitigation of Cr evaporation in these coated systems have been evaluated. Unlike conventional single-composition coating studies, we establish a compositional-complexity-controlled design axis (ternary → quaternary → quinary) for sputtered metallic precursors that oxidize into spinel-dominant scales at 650 °C, and show that suppressing early-stage Fe ingress stabilizes a dense single-spinel layer, enabling simultaneous improvement in ASR and Cr-volatilization durability.

## 2. Methods

### 2.1. Target preparation

Equimolar Fe-Mn-Co, Fe-Mn-Co-Cu, and Fe-Mn-Co-Cu-Ni alloy targets were prepared by vacuum arc melting. The purity of all raw materials was better than 99.9 % and Ti getter was used. After melting, each ingot was machined into a disc-shaped target with a diameter of 3 inches and a thickness of 4 mm. The elemental composition of each alloy target was analyzed by X-ray fluorescence (XRF, Hitachi EA1400).

### 2.2. Coating preparation

In this study, commercially available SUS430 stainless steel was used as the substrate for the coating process. The chemical composition of the SUS430 substrate used in this study was analyzed via ICP-MS (Thermo Fisher Scientific iCAP TQ), as shown in the Supplementary Table S1. The quantitative analysis of the ferritic stainless steel substrate confirmed a composition of 16.37 wt. % Cr and 0.391 wt. % Mn, with Fe comprising approximately 80.41 wt. %. These results align the substrate chemistry closely with AISI 430 standards, showing consistent results with the reference values from the MatWeb database [31]. Each sample was cut into size of 10 mm × 10 mm × 0.3 mm, followed by grinding and polishing with 0.05 μm $Al_2O_3$ suspension. The surface roughness of each sample measured by Alpha-step was 22.5 nm in average. The target elements were deposited onto the substrate via magnetron sputtering process (Sputter system, ULVAC RFS-200S). For each target, the sputtering parameters were kept the same. The Ar pressure was maintained at $2.4 \times 10^{-3}$ torr, and the Ar flow rate was kept at 30 sccm. The sputtering power was 150 W and a bias of −95 V was applied. The sputtering deposition was carried out at room temperature for 1 h to obtain a single-sided coating with an average thickness of 800 nm. Hereafter, Fe-Mn-Co, Fe-Mn-Co-Cu, and Fe-Mn-Co-Cu-Ni-coatings are, respectively, denoted as Coatings 1, 2, and 3.

### 2.3. Isothermal oxidation tests

The isothermal oxidation tests of coated and uncoated steels were conducted in the box furnace with $Al_2O_3$ fiber board insulation. To accurately capture the intrinsic oxidation kinetics, specimens were placed in high-purity dense $Al_2O_3$ crucibles. This setup ensures chemical inertness and maintains a stable gas-specimen equilibrium by minimizing the potential getter effect of surrounding materials on Cr species [32]. The specimens were heated to 650 °C by 5 °C/min, held at 650 °C for 24, 124, 324, 524 h, followed by air cooling. The weight of each sample was measured by using electronic weighting balance with sensitivity down to $10^{-5}$ g. In this study, mass change was defined as the weight difference of the specimen itself; thus, each specimen was weighed independently of its crucible after each oxidation interval. And mass gain was calculated by subtracting the initial weight from the oxidized weight of each sample. The average mass gain and standard deviation for each oxidation interval were calculated from three replicate samples. The oxidation mass gain curve was plotted and the microstructure of oxide scales were analyzed.

### 2.4. Area specific resistance measurement

The coated steels with different exposure time were used to measure the ASR value. Four-probe method was utilized to measure the resistance of each sample in a 650 °C-furnace. Gold wires were used as conductive wires during the measurement, and silver paste was used to sinter the sample and the gold wires. Keysight E3634A was used to record the electrical resistance. The experimental ASR value was determined by applying the following equation:

$$ASR\left(m\Omega{\cdot}cm^2\right) = R{\cdot}\frac{A}{2} \quad (1)$$

Where R (mΩ) represents the measured resistance of the sample, A ($cm^2$) is the area coated with silver paste, and a coefficient of 2 is used to normalize the resistance of the oxide scales formed on both sides of the sample.

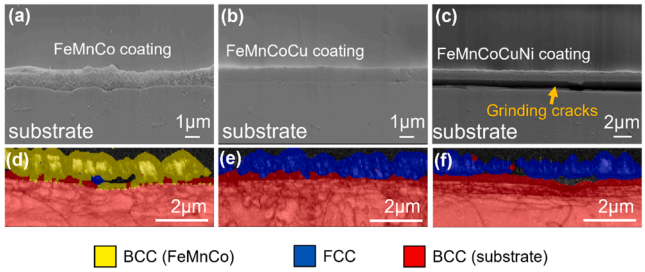


**Fig. 1.** Cross-sectional morphology and EBSD phase identification of the as-coated steels: (a,d) Fe-Mn-Co coated steel, (b,e) Fe-Mn-Co-Cu coated steel, (c, f) Fe-Mn-Co-Cu-Ni coated steel.

### 2.5. Cr evaporation test

The Cr evaporation test was conducted following the procedures described in the literature [33]. The degree of Cr evaporation in each sample was analyzed in the box furnace, and a CaO coated $Al_2O_3$ plate was placed 1 mm above each sample. Once the Cr evaporated and reacted with the CaO coating, the formation of Ca-containing green--color chromate could be detected. Following the 524-hour oxidation test, a Cr evaporation test was conducted on each material at 650 °C for 100 h, with the ambient humidity kept at approximately 40 % RH. And the light to dark green-color contrast of the chromate formed on each $Al_2O_3$ plate could be a basis for judging the evaporation of Cr. And the X-ray fluorescence was used to detected the content of Cr on the plate. To ensure the repeatability and fairness of the comparison, all coated and uncoated samples were tested simultaneously in the same batch. Furthermore, the tests were performed in two independent batches for the coated samples.

### 2.6. Characterization

The microstructures of the oxide scales formed on samples were analyzed by scanning electron microscope (SEM, Zeiss Gemini 300 Scanning Electron Microscope). The elemental distributions across the oxide scales were analyzed by using energy dispersive X-ray spectrometer (EDS, Oxford Instrument ULTIM Max 40). The cross-sectional phase structures of the samples were identified by electron backscattered diffraction analysis (EBSD, Oxford Instrument Symmetry S2). Focused Ion Beam lift-out techniques (FIB, FEI Helios Nanolab 600i System) were employed to prepare specimens to be analyzed by Transmission Electron Microscopy (TEM, JEOL JEM-F200) equipped with Energy-Dispersive X-ray Spectroscopy (EDS) to provide detailed microstructural and compositional information. Scanning Transmission Electron Microscopy (STEM) bright field images and corresponding Selected Area Electron Diffraction (SAED) patterns were acquired to comprehensively examine the phase structure of the coated steels. The phase structures of the samples were also identified by using the X-ray Diffractometer (BRUCKER D2 Phaser). The Cu (Kα radiation = 1.54056 Å) radiation was operated at 30 kV and 20 mA, and the diffraction angle (2θ) was from 20° to 100° at a scanning speed of 2°/min. The surface elemental composition and chemical valence states of the 24 h and 524 h oxidized samples were analyzed by X-ray photoelectron spectroscopy (XPS, ULVAC-PHI 5000 Versaprobe II). The binding energy was calibrated to the C 1 s peak at 284.8 eV.

## 3. Results

### 3.1. Microstructure of the as-coated samples

The cross-sectional morphology and EBSD phase identification of the as-coated steels are illustrated in Fig. 1. The three coatings have an average thickness of 800 nm. The EBSD results confirmed that SUS430 substrate exhibit a body-centered cubic (BCC) structure. The as-sputtered Fe-Mn-Co (Coating 1) showed a BCC structure via EBSD, while the Fe-Mn-Co-Cu (Coating 2) and Fe-Mn-Co-Cu-Ni (Coating 3) coatings exhibited face-centered cubic (FCC) structures. The elemental composition of each coating, as detected from the cross-sectional surface of the coated steels by SEM-EDS, is listed in Table 1. The variations in sputter yield among the constituent elements are likely associated with competitive sputtering and re-sputtering behaviors driven by the distinct surface binding energies of the elements [34,35].

**Table 1**
Elemental composition of alloy coatings (at%).

| | Fe | Mn | Co | Cu | Ni |
|---|---|---|---|---|---|
| Coating 1 | 37.3 ± 0.25 | 25.0 ± 0.15 | 37.7 ± 0.23 | / | / |
| Coating 2 | 24.8 ± 0.18 | 22.6 ± 0.03 | 22.5 ± 0.03 | 30.1 ± 0.26 | / |
| Coating 3 | 21.7 ± 0.53 | 16.2 ± 0.23 | 20.7 ± 0.55 | 21.4 ± 0.15 | 20.0 ± 0.12 |

### 3.2. Microstructure of the oxidized samples

Fig. 2 presents the cross-sectional microstructure, EDS line scan, and EBSD results of oxide scales formed on the three coated steels after 24 h of oxidation test. As shown in Fig. 2a, Coating 1 coated steel displayed a non-uniform oxide scale characterized by distinct thin and thick regions. The magnified images reveal that the thickness of thin regions was approximately 5 μm, while the thick regions reached a depth of about 9 μm. The EDS analysis of the elemental distribution across thick regions of the oxide scale, as shown in Fig. 2d, demonstrates a multi-layered oxide structure. An outer Fe-Mn-Co oxide layer, approximately 3 μm thick, was identified. Beneath this layer was an approximately 3-μm-thick Fe-rich oxide layer, followed by Cr-Fe oxide structures with an average thickness of 2.7 μm and an innermost 700-nm-thick Cr-rich oxide scale. The thin regions of oxide scales also exhibited a multi-layered structure with a 3-μm-thick Fe-Mn-Co oxide layer on top, an underlying 1.8-μm-thick Fe-rich oxide layer, and a 300-nm-thick Cr-rich oxide layer at the coating/substrate interface. Similar to Coating 1, non-uniform oxide scales were observed on Coating 2 coated steel, as depicted in Fig. 2b. The oxide layer thickness varied significantly, with the thin regions of approximately 3 μm and the thick regions reaching a depth of about 6.5 μm. The oxide scales in thick regions exhibited a multi-layered elemental distribution, as revealed by the EDS analysis shown in Fig. 2e. The outermost layer, approximately 2.5 μm thick, was a mixed oxide layer of Fe, Mn, Co, and Cu. Beneath this layer was a 2 μm-thick Fe oxide layer, followed by Cr-Fe oxide structures with an average thickness of 1.1 μm. The innermost layers consisted of Cr-rich oxide layers with a thickness of approximately 700 nm. For the thin regions of oxide scales, the result indicates a 2-μm-thick top Fe-Mn-Co-Cu oxide layer, an underlying Fe-rich oxide layer with a thickness of 0.5 μm, and an innermost 300-nm-thick Cr-rich oxide layer. In contrast to Coatings 1 and 2, the oxide scales formed on Coating 3 coated steels, as illustrated in Fig. 2c, displayed a distinct structure and a uniform thickness of approximately 2 μm. Fig. 2f indicates that a relatively uniform elemental distribution within the oxide layer, with only a thin (approximately 300 nm) accumulation of Cr-rich oxide at the coating/substrate interface. As shown in Fig. 2g and h, the EBSD results indicate that the outermost Fe-Mn-Co and Fe-Mn-Co-Cu oxide layers in Coating 1 and Coating 2 coated steels, respectively, displayed a spinel structure. The Fe-rich oxide layers, present in the oxide scales of both samples, exhibited a hematite structure. However, the Cr-Fe oxides and the innermost Cr-rich oxide layer were not detectable by EBSD analysis (dark regions between hematite and BCC substrate), likely due to their extremely fine grain size, which exceeded the resolution limit of the EBSD technique. For Coating 3 coated steel, the EBSD analysis in Fig. 2i reveals that its oxide scale

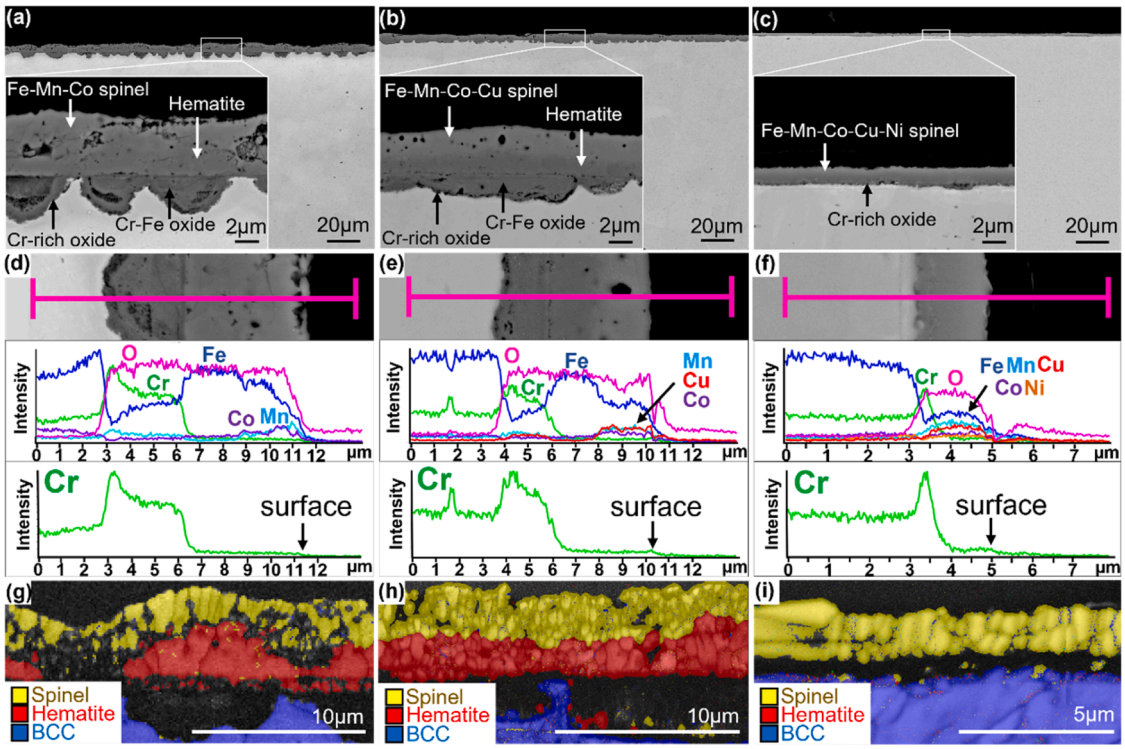


**Fig. 2.** Cross-sectional morphology, EDS line-scan analysis and Cr content profile, and EBSD analysis of the oxide scales after 24 h of oxidation test: (a, d, g) Coating 1 coated steel;(b, e, h) Coating 2 coated steel; (c, f, i) Coating 3 coated steel.

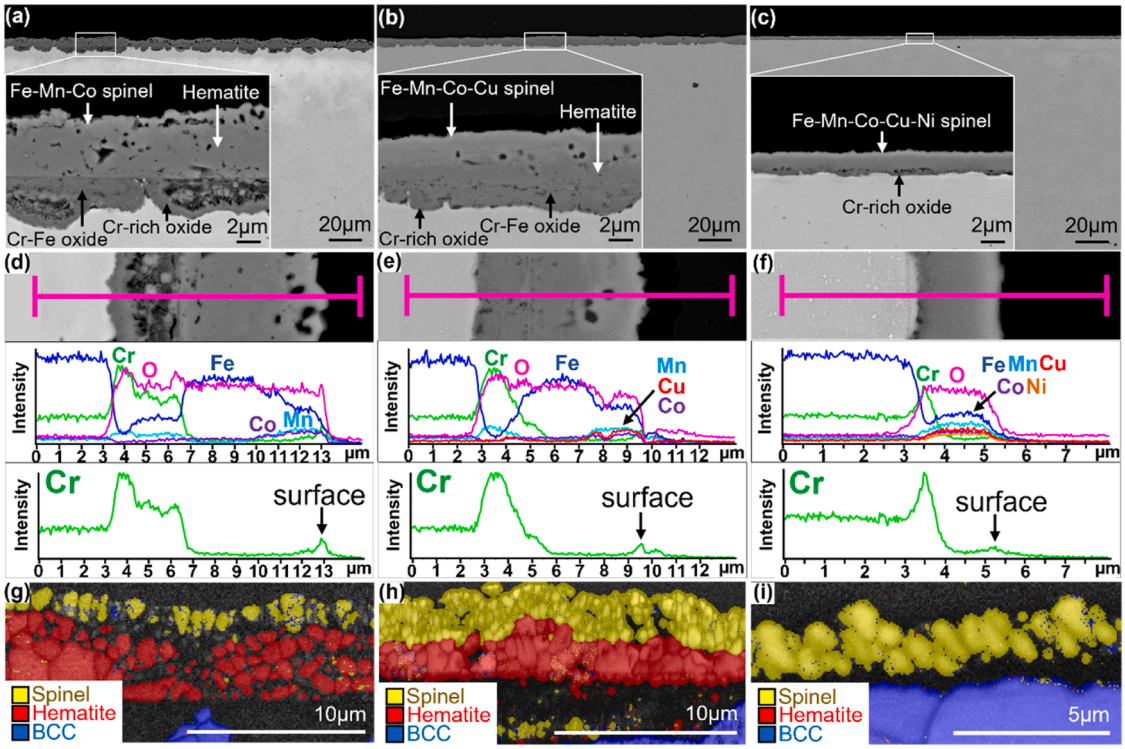


**Fig. 3.** Cross-sectional morphology, EDS line-scan analysis and Cr content profile, and EBSD analysis of the oxide scales after 524 h of oxidation test: (a, d, g) Coating 1 coated steel;(b, e, h) Coating 2 coated steel; (c, f, i) Coating 3 coated steel.

with a uniform elemental distribution was mainly a single-phase spinel structure. Comparing the densities of oxide scales among the three coatings, Coating 3 exhibits a denser microstructure throughout its oxide scale. In contrast, the oxide scales of Coating 1 and Coating 2 display higher porosity, localized at both the outer spinel/hematite layers and within the inner Cr-Fe oxides.

Regarding the long-term stability of the oxide scales, the samples were examined after extended oxidation periods. The microstructure of

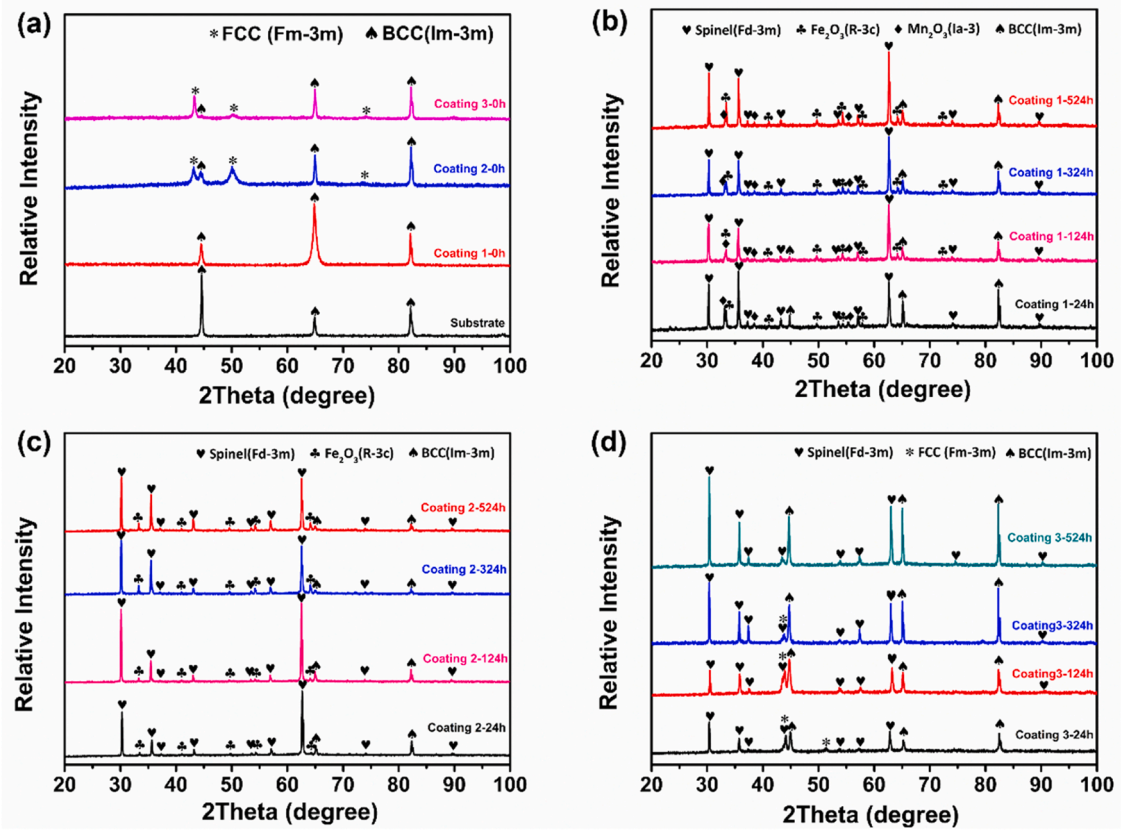


**Fig. 4.** XRD patterns of (a) the uncoated substrate (0 h) and the as-coated samples (0 h), and (b–d) the coated specimens after various oxidation durations (24, 124, 324, and 524 h) for (b) Coating 1, (c) Coating 2, and (d) Coating 3.

the uncoated steel after 500 h is provided in Supplementary Figure S1, which shows the formation of $Cr_2O_3$ scale with a Mn-rich surface layer (Mn-Cr spinel), reaching an average total thickness of approximately 600 nm after 500 h of oxidation. This oxide structure formed on uncoated SUS430 at 650 °C is consistent with observations reported in the literature [36]. Fig. 3 presents the microstructure of the three coated steels after 524 h of oxidation test at 650 °C. For the coated steels, although there were no apparent differences in the morphology and thickness of oxide scales after the 524-hour oxidation test, Cr distribution varied with oxidation time. As depicted in Fig. 3d and e, EDS results reveal the significant accumulation of Cr content on the outer spinel surfaces in Coatings 1 and 2 coated steels after the long-term exposure. In contrast, no obvious increase in Cr content was observed on the oxide scale surface of the Coating 3 coated steel compared to its as-prepared condition, as shown in Fig. 3f. Indeed, during extended oxidation, the concentration of volatile Cr species within the furnace may reach a sufficiently high level. Upon opening the furnace for sample retrieval, the rapid cooling triggers the condensation of these gaseous species onto the sample surfaces. However, the distinct Cr levels observed among the coatings suggest that this phenomenon is dominated by local Cr vapor pressures, reflecting inherent differences in the coatings' evaporation behavior. EBSD analysis revealed that the oxide scales of Coating 1 and Coating 2 coated steels maintained a multi-phase structure throughout the 524-hour exposure period, whereas the oxide scale of Coating 3 coated steel consistently exhibited a single spinel structure throughout the oxidation process. Furthermore, no evidence of blistering or spallation was observed for any of the three coated steels after both 24 and 524 h of oxidation. This indicates robust interfacial adhesion of the coatings and oxide scales throughout the test duration, as confirmed by the edge and top-view images provided in Supplementary Figure S2.

To clarify the phase transformation process during long-term oxidation, the XRD patterns of the uncoated substrate (0 h), the as-coated samples (0 h), and the coated specimens after various oxidation durations (24, 124, 324, and 524 h) are presented in Fig. 4. The XRD analysis identifies the BCC phase (Im-3 m, JCPDS No. 6–696) as the primary constituent of the uncoated substrate. For Coating 1, the as-deposited layer also exhibits a BCC structure, with no additional phases detected. In contrast, Coatings 2 and 3 comprise an FCC phase (Fm-3 m, JCPDS No. 4–836) in addition to the BCC substrate. The phase structures of the alloy coatings are consistent with the EBSD results (Fig. 1). Following the oxidation tests, the phase evolution of the coated steels was characterized. For Coating 1 coated steels, the main phases identified throughout the oxidation periods were $CoFe_2O_4$ (Fd-3 m) and $Fe_2O_3$ (R-3c) with JCPDS No. 22–1086 and 33–664, respectively. These detected phases corresponded to the Fe-Mn-Co spinel structure and the hematite structure in the oxide scales of Coating 1 coated steels. Additionally, $Mn_2O_3$ (bixbyite, Ia-3) phases corresponding to JCPDS No. 89–2809 were identified. For Coating 2 coated steels, the main phases identified throughout the oxidation periods were $CuFe_2O_4$ (Fd-3 m) and $Fe_2O_3$ (R-3c) with JCPDS No. 77–10 and 33–664, respectively. These identified phases corresponded to the Fe-Mn-Co-Cu spinel structure and the hematite layer within the oxide scales, with the latter exhibiting a progressive increase in diffraction intensity over time. For Coating 3 coated steels, the main phases identified throughout the oxidation periods were $CuFe_2O_4$ (Fd-3 m) with JCPDS No. 77–10. This identified phase corresponded to the primary Fe-Mn-Co-Cu-Ni spinel structure in the oxide scales of Coating 3 coated steels. Some residual FCC peaks were detected in the 24 h sample of Coating 3. These peaks indicate the presence of the residual HEA coating, which progressively diminished as the oxidation duration increased. The Rietveld-refined XRD patterns and the relative volume fractions of oxide phases for the 24 h and 524 h oxidized coated samples are presented in the Supplementary Figure S3 and Supplementary Table S2. The quantitative analysis confirms that while Coatings 1 and 2 exhibited a gradual increase in the hematite

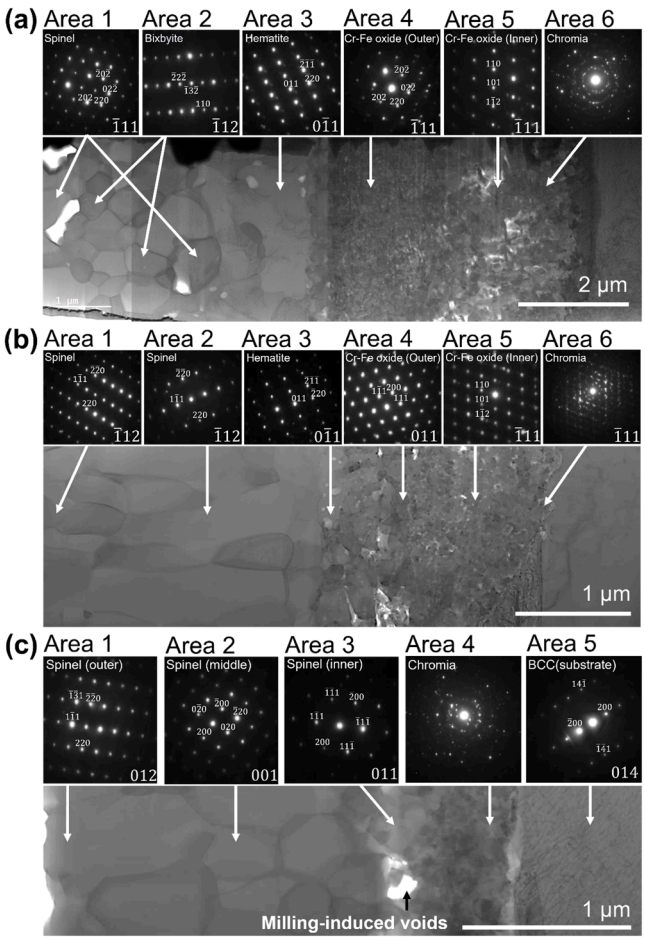


**Fig. 5.** STEM bright field images with corresponding SAED patterns of the oxide scales (cross-sectional view) for (a) Coating 1, (b) Coating 2, and (c) Coating 3.

phase over time, Coating 3 maintained a remarkably stable, near-pure spinel phase even after long-term oxidation.

Fig. 5 presents the TEM characterization of oxide scales formed on the three coated steels following 524 h of oxidation. As shown in Fig. 5a for Coating 1 coated steel, the SAED pattern of area 1 indexed an FCC spinel structure along the [$\bar{1}$11] zone axis. EDS analysis revealed its composition in the outer and inner region to be $Fe_{26.3}Co_{14.5}Mn_{6.7}Cr_{4.5}O_{48.2}$ and $Fe_{27.4}Co_{14.8}Mn_{7.1}Cr_{1.2}O_{49.5}$, respectively. Additionally, some BCC bixbyite grains, indexed along the [$\bar{1}$12] zone axis, were detected intergranularly within the Fe-Mn-Co spinel grains. These bixbyite grains were likely not detected by EBSD analysis due to their smaller grain size. Large pores were clearly observed in the spinel/bixbyite mixed oxide layer. The pattern of area 3 was indexed to reflections of corundum structure along the [011] zone axis, which corresponds to the hematite phase shown in the EBSD results. Beneath this hematite phase, the fine-grained Cr-Fe oxides exhibit a double-layered and porous oxide structure. The pattern of the outer layer (area 4) indexed a spinel structure along the [$\bar{1}$11] zone axis, and that of the inner layer (area 5) indexed a corundum structure along the [$\bar{1}$11] zone axis. Combined with the EDS results, each of the Cr-Fe oxides were determined to consist of an outer $Fe_{26.6}Cr_{15.2}Mn_{2.1}O_{54.9}$ spinel and an inner $Cr_{28.0}Fe_{10.6}Mn_{4.9}Co_{2.6}O_{54.1}$ corundum. Furthermore, the SAED pattern of the innermost area displayed a ring pattern, which corresponds to nano-grained corundum (chromia, $Cr_{38.0}Fe_{4.6}Mn_{2.0}O_{54.7}$) according to the inter-ring distance. As shown in Fig. 5b for Coating 2 coated steel, the pattern of area 1 indexed a spinel structure along the [$\bar{1}$12] zone axis, and the same structure was indexed for area 2. The spinel layer in area 1 exhibited a composition of $Fe_{22.5}Cu_{8.5}Mn_{6.9}Co_{5.7}Cr_{2.2}O_{54.2}$, while its composition in area 2 was $Fe_{23.6}Cu_{9.0}Mn_{7.0}Co_{5.5}Cr_{0.45}O_{54.5}$, which were similar. Similarly, the diffraction pattern of area 3 was indexed to corundum along the [0$\bar{1}$1] zone axis, corresponding to the hematite phase. The patterns of areas 4 and 5 were indexed to spinel along the [011] zone axis and corundum along the [$\bar{1}$11] zone axis, respectively. These correspond to porous $Fe_{20.6}Mn_{1.4}Cr_{15.7}O_{60.8}$ spinel and $Cr_{23.0}Fe_{9.0}Mn_{1.5}Co_{5.0}Cu_{3.1}O_{60.8}$ corundum. And the pattern of the innermost layer corresponds to corundum (chromia, $Cr_{32.3}Fe_{6.4}Mn_{2.1}O_{58.1}$) along the [$\bar{1}$11] zone axis, exhibiting a partial ring pattern. As shown in Fig. 5c for Coating 3 coated steel, the SAED patterns of areas 1, 2, and 3 were indexed to spinel along the [012], [001], and [011] zone axis, respectively. The outer and inner areas of the spinel exhibited homogeneous compositions of $Fe_{15.9}Cu_{8.7}Mn_{8.8}Co_{7.8}Ni_{3.1}Cr_{1.9}O_{53.5}$ and $Fe_{16.3}Cu_{7.9}Mn_{7.5}Co_{7.7}Ni_{3.9}Cr_{3.1}O_{53.6}$, respectively. Beneath the spinel, the SAED pattern of the innermost oxide (area 4) displayed a diffraction ring corresponding to corundum (chromia, $Cr_{29.6}Fe_{7.8}Mn_{1.5}Cu_{2.7}Co_{1.5}O_{57.1}$).

### 3.3. XPS analysis

Fig. 6 presents the high-resolution XPS spectra obtained from the surface of the three coated steels after 24 h of oxidation. Corresponding spectra for the samples oxidized for 524 h are provided in the Supplementary Figure S4. The calculated surface elemental compositions and the detailed valence states of the coating elements are summarized in Supplementary Table S3 and Table 2, respectively. The Fe 2p spectra reveal the presence of $Fe^{2+}$ (~710.3 and 722.8 eV) and $Fe^{3+}$ (~713.0 and 724.4 eV), corresponding to the $2p_{3/2}$ and $2p_{1/2}$ peaks, respectively; these results are in good agreement with the study by Zhao et al. [24]. Three distinct satellite peaks located at approximately 714.8 eV, 718.3 eV, and 729.6 eV are also observed, consistent with the findings of Yamashita et al. [37]. Regarding the Mn species, the Mn $2p_{3/2}$ peaks are deconvoluted into $Mn^{2+}$ (~640.1 eV), $Mn^{3+}$ (~641.6 eV), and $Mn^{4+}$ (~643.2 eV), following the literatures reported for Mn-Co systems [38, 39]. Furthermore, the Mn $2p_{1/2}$ peaks are located approximately 11.6 eV higher in binding energy, which is consistent with the study by Ramana et al. [40]. Notably, the satellite feature at ~647 eV confirms the existence of $Mn^{2+}$. Quantitative results in Supplementary Table S3 show that the surface Mn concentration of Coating 1 surpasses the actual spinel stoichiometry determined by TEM, confirming the substantial presence of the Mn-rich bixbyite phase. In Coating 1, the predominance of the bixbyite phase introduces a high concentration of $Mn^{3+}$ (~49 %) after 24 h of oxidation. Interestingly, after 524 h of oxidation, although the surface Mn content in Coating 1 significantly decreases—suggesting the partial incorporation of the bixbyite phase into the spinel lattice—the $Mn^{3+}$ fraction shows no marked decrease. This implies that $Mn^{3+}$ remains the predominant species within the Coating 1 system, even as the phase distribution evolves. In contrast, as the system transitions to Coating 2 and Coating 3, the $Mn^{3+}$ content decreases while $Mn^{2+}$ increases; meanwhile, the $Mn^{4+}$ fraction remains stable or slightly increases. This shift results in a more homogeneous distribution of Mn ions, which closely reflects the intrinsic Mn configuration within their respective spinel structures. Furthermore, the Mn peaks in Coatings 2 and 3 exhibit a shift toward higher binding energies compared to Coating 1. This evolution is attributed to the alleviation of structural distortion (associated with the Jahn-Teller effect) as the $Mn^{3+}$ concentration declines, leading to a more compact spinel configuration. As for the Co species, the Co 2p spectra reveal the presence of $Co^{3+}$ (~780.0 and 795.8 eV) and $Co^{2+}$ (~782.1 and 797.5 eV), corresponding to the $2p_{3/2}$ and $2p_{1/2}$ peaks, respectively. These doublets are accompanied by two distinct satellite peaks at approximately 786.6 eV and 802.9 eV. As the system transitions from Coating 1 to Coating 3, the $Co^{3+}/Co^{2+}$ ratio increases significantly from 0.52, 0.56, to 0.79, respectively (based on 524 h oxidation). The Cu 2p spectra of Coatings 2 and 3 are

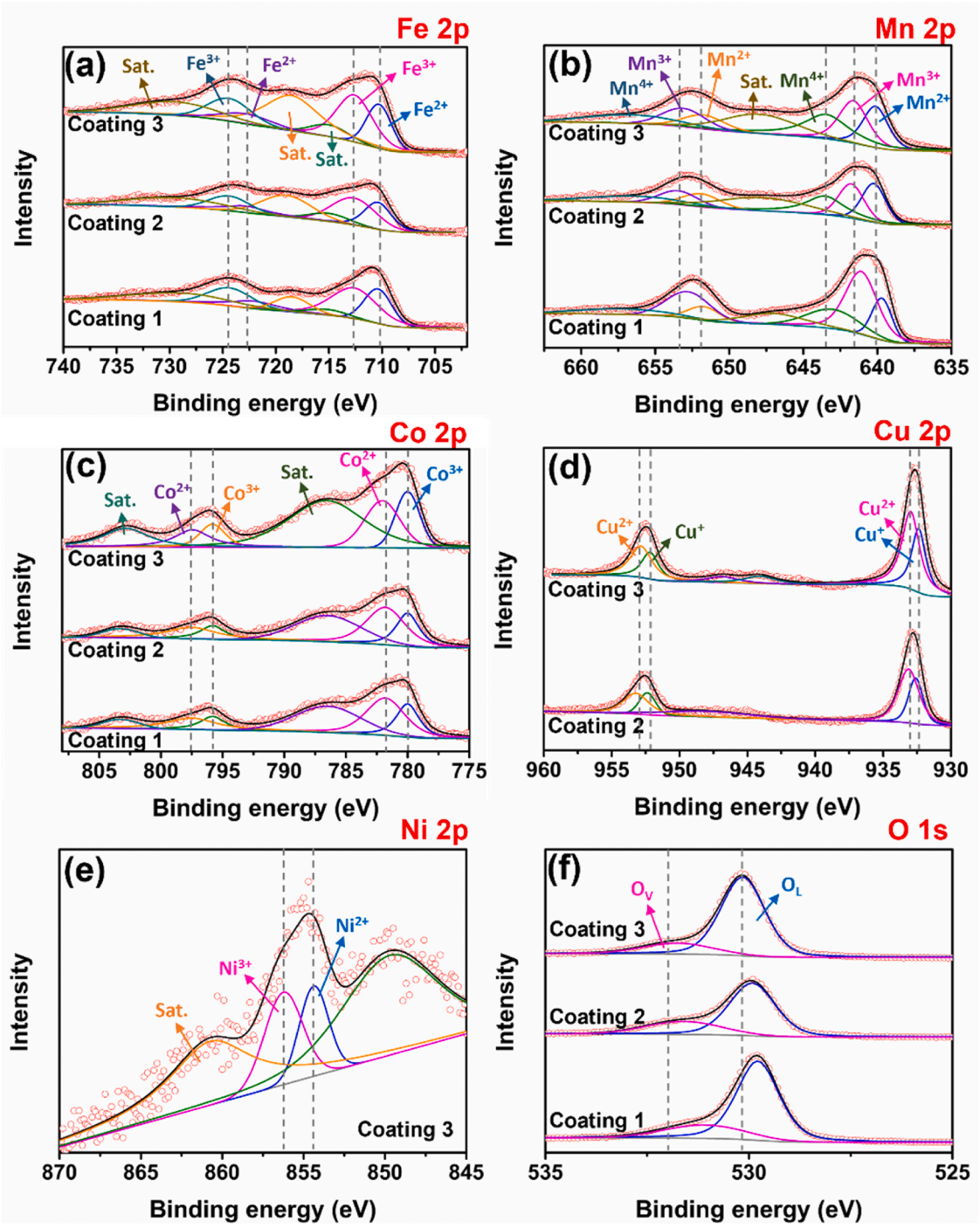


**Fig. 6.** High-resolution XPS spectra of Coatings 1, 2, and 3 coated steel after 24 h of oxidation: (a) Fe 2p, (b) Mn 2p, (c) Co 2p, (d) Cu 2p, (e) Ni 2p, (f) O 1 s.

**Table 2**
Chemical state evolution of the coating elements in Coating 1 (C1), Coating 2 (C2), and Coating 3 (C3) after 24 and 524 h of oxidation.

| | Fe 2p | | Mn 2p | | | Co 2p | | Cu 2p | | Ni 2p | | O 1s | |
|---|---|---|---|---|---|---|---|---|---|---|---|---|---|
| | $Fe^{2+}$ | $Fe^{3+}$ | $Mn^{2+}$ | $Mn^{3+}$ | $Mn^{4+}$ | $Co^{2+}$ | $Co^{3+}$ | $Cu^{+}$ | $Cu^{2+}$ | $Ni^{2+}$ | $Ni^{3+}$ | $O_L$ | $O_V$ |
| C1–24h | 37.8 % | 62.2 % | 17 % | 49 % | 34 % | 74 % | 26 % | / | / | / | / | 72 % | 28 % |
| C1–524h | 42.1 % | 57.9 % | 19 % | 48 % | 33 % | 66 % | 34 % | / | / | / | / | 68 % | 32 % |
| C2–24h | 35.3 % | 64.7 % | 31 % | 36 % | 33 % | 65 % | 35 % | 37 % | 63 % | / | / | 67 % | 33 % |
| C2–524h | 44.2 % | 55.8 % | 26 % | 36 % | 38 % | 64 % | 36 % | 42 % | 58 % | / | / | 74 % | 26 % |
| C3–24h | 37.1 % | 62.9 % | 27 % | 37 % | 36 % | 55 % | 45 % | 38 % | 62 % | 42.7 % | 52.3 % | 82 % | 18 % |
| C3–524h | 41.3 % | 58.7 % | 24 % | 38 % | 38 % | 56 % | 44 % | 42 % | 58 % | 40.1 % | 59.9 % | 79 % | 21 % |

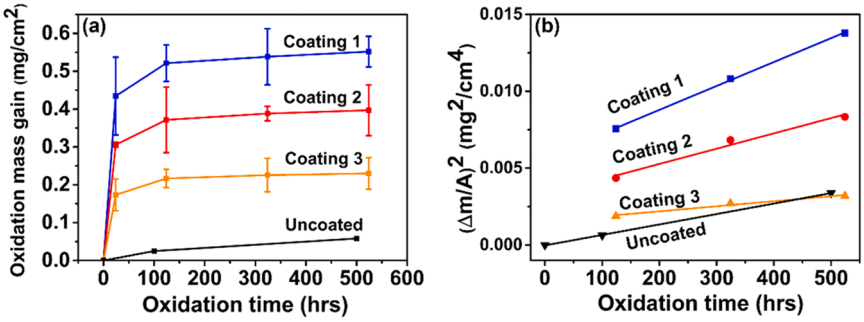


**Fig. 7.** (a) Oxidation mass gain and (b) squared mass gain of uncoated-, Coating 1-, Coating 2-, and Coating 3 coated steels.

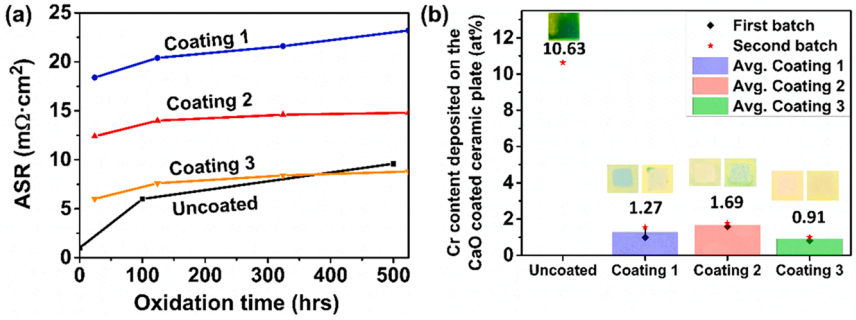


**Fig. 8.** (a) ASR values of the uncoated SUS430 and the samples coated with Coating 1, Coating 2, and Coating 3 measured at 650 °C after varying oxidation testing times. (b) XRF analysis of the amount of Cr content deposited on the CaO coated ceramic plates after the Cr evaporation test for 100 h at 650 °C.

characterized by peaks for $Cu^{+}$ (~932.4 and 952.2 eV) and $Cu^{2+}$ (~933.0 and 952.9 eV), which are assigned to the $2p_{3/2}$ and $2p_{1/2}$ states, respectively. These peak assignments for both Co and Cu are in good agreement with the results reported by Zhao et al. [24]. Regarding the Ni species present in Coating 3, the Ni $2p_{3/2}$ spectra are characterized by peaks at ~854.3 eV and ~856.2 eV, along with a satellite peak at ~862.5 eV. These features correspond to $Ni^{2+}$ and $Ni^{3+}$ states, respectively, and are consistent with reports on Ni-Mn-Co spinel powders [39]. The observed peak at a lower binding energy, compared to standard Ni $2p_{3/2}$ position, may be attributed to spectral interference of other constituent elements. In addition to the metallic species, the O 1 s spectra were also investigated. The O 1 s spectra of the three coatings are characterized by two main components: lattice oxygen ($O_L$) at ~529.9–530.4 eV and vacancy oxygen ($O_V$) at ~531.3–531.8 eV, both of which are in good agreement with the literature [24]. Notably, the O 1 s peaks exhibit a gradual shift toward higher binding energies from Coating 1 to Coating 2 and finally Coating 3, reflecting shorter metal-oxygen (M-O) bonds and stronger electronic interactions in the lattice. Furthermore, Coating 3 exhibits the highest $O_L/O_V$ ratio among the three coatings throughout the oxidation process.

### 3.4. Oxidation mass gain

Fig. 7a presents the oxidation mass gain curves of coated and uncoated samples during the 524-hour oxidation test (500 h for the uncoated steel) at 650 °C. All coated steels exhibited a large mass gain during the first 24 to 124 h of oxidation test, followed by a gradual increase up to 524 h. Coating 1- and Coating 2 coated steels exhibited significantly larger mass gain compared to Coating 3 coated steel during the early oxidation stage. From 124 to 524 h of oxidation, a parabolic relationship was observed between mass change and time, as shown below:

$$\left(\frac{\Delta m}{A}\right)^2 = k_p t \quad (2)$$

where $\Delta m$(mg) represents the sample mass gain, A(cm$^2$) is the sample surface area, t(s) is the oxidation testing time, and $k_p$ denotes the parabolic rate constant, which is the slope of the fitting line in Fig. 7b. Based on parabolic trend fitting (Fig. 7b), Coatings 1, 2, and 3 coated steels, as well as the uncoated steel, exhibited the oxidation rate constants of $4.32 \times 10^{-15}$ $g^2cm^{-4}s^{-1}$, $2.76 \times 10^{-15}$ $g^2cm^{-4}s^{-1}$, $9.09 \times 10^{-16}$ $g^2cm^{-4}s^{-1}$, and $1.89 \times 10^{-15}$ $g^2cm^{-4}s^{-1}$, respectively.

### 3.5. Area specific resistance

Fig. 8a presents the experimental ASR values for each group of samples. Throughout the oxidation testing period, the ASR values of all coated samples followed a general trend of Coating 1 > Coating 2 > Coating 3. After 524 h of oxidation test, the ASR values of Coating 1-, Coating 2-, and Coating 3 coated steels are 23.2, 14.8, and 8.8 mΩ·cm$^2$, respectively. The uncoated steel suffered from a significant resistance increment during high-temperature oxidation. Although its initial ASR is lower than that of the coated samples, the ASR of the uncoated substrate increases rapidly to 9.6 mΩ·cm$^2$ after 500 h. This value is consistent with the typical ASR evolution for uncoated SUS430 at 650 °C reported in the literature [36].

### 3.6. Cr evaporation test

Fig. 8b presents the Cr evaporation content for each sample group during the Cr-evaporation test, as well as the corresponding color changes of the ceramic plate caused by Cr deposition and reaction. For the uncoated steel, the Cr deposition on the ceramic plate measured was 10.63 at %. In comparison, the average Cr contents for Coating 1, Coating 2, and Coating 3 were 1.27, 1.69, and 0.91 at %, respectively, with consistent results observed across both batches. The uncoated steel exhibited ten times higher Cr evaporation rate at 650 °C compared to those of three coated systems. The color contrast of the ceramic plates also confirmed the significantly higher Cr evaporation from the bare steel. This indicates that all the three coatings were effective in retarding

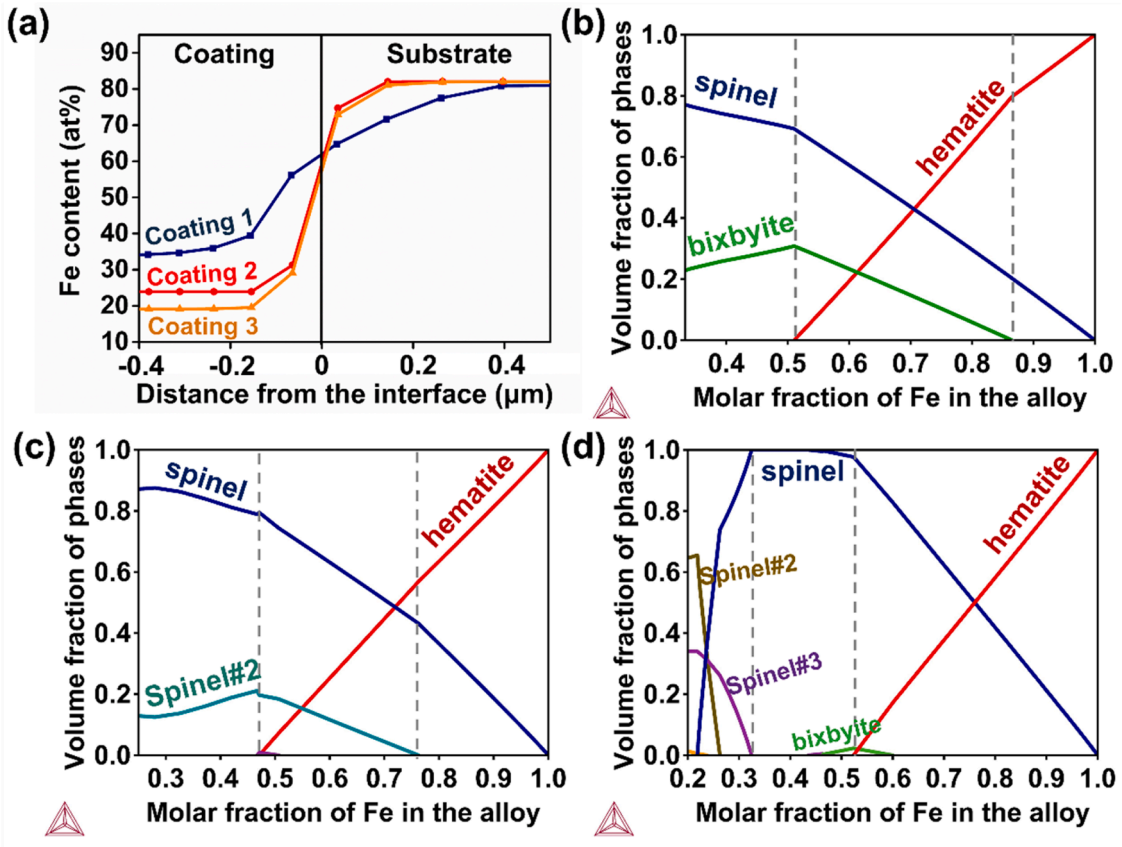


**Fig. 9.** (a) Thermo-Calc DICTRA simulation of Fe diffusion behavior across the coatings/substrate interface at 650 °C for 30 min (TCFE 11, MOBFE 6 database); Thermo-Calc simulation of (b) $Fe_x(Mn_{25.0}Co_{37.7})_{1-x}$, (c) $Fe_x(Mn_{22.6}Co_{22.5}Cu_{30.1})_{1-x}$, (d) $Fe_x(Mn_{16.2}Co_{20.7}Cu_{21.4}Ni_{20.0})_{1-x}$ oxidation phases (fully oxidized) at 650 °C (TCOX 12 database).

**Table 3**
Summary of oxide layer resistivity [46–48], thickness, and calculated ASR for all samples after 650 °C oxidation test for 524 h.

| Coating | Thickness of each oxide layer (μm) without spinel | | | | ASR (mΩ $cm^2$) | |
|---|---|---|---|---|---|---|
| | $Cr_2O_3$ | $(Cr,Fe)_2O_3$ | $(Cr,Fe)_3O_4$ | $Fe_2O_3$ | Calculated | Experimental |
| Coating1(thick area) | 0.7 ± 0.2 | 1.4 ± 0.6 | 1.4 ± 0.4 | 3.0 ± 0.5 | 38.67 | 23.2 |
| Coating1(thin area) | 0.3 ± 0.05 | / | / | 1.8 ± 0.3 | 12.71 | |
| Coating2(thick area) | 0.7 ± 0.04 | 0.6 ± 0.2 | 0.5 ± 0.2 | 2.0 ± 0.2 | 28.78 | 14.8 |
| Coating2(thin area) | 0.3 ± 0.05 | / | / | 0.5 ± 0.1 | 9.44 | |
| Coating3 | 0.3 ± 0.08 | / | / | / | 8.19 | 8.8 |
| Resistance (ohm cm) | 273 [46] | 35.8 (calculated) | 50.1 [47] | 25.1 [48] | | |

evaporation and diffusion of Cr.

## 4. Discussion

### 4.1. Microstructure evolution from metals to oxides

Significant microstructural differences were observed among the oxide layers of the three coated samples. The multilayer oxide structure can be broadly categorized as follows: an outermost Cr-lean spinel oxide layer; an intermediate hematite layer observed only in Coatings 1 and 2; inner Cr-Fe oxide structures, found in thick regions of the oxide scales of Coatings 1 and 2;and an innermost $Cr_2O_3$-rich corundum layer. Fe exerted a significant influence on the oxidized microstructure of coatings 1 and 2, which was evident in the formation of hematite phases and the markedly higher Fe content within the Cr-lean spinel layer compared to other metal ions. It is believed that during the initial oxidation stage, while the coatings remained in the metallic state, Fe diffused into the coating layer due to a concentration gradient at the substrate/coating interface. This occurred before a continuous $Cr_2O_3$ diffusion barrier formed. However, this phenomenon was not as obvious in Coating 3 as it was in Coatings 1 and 2, which was evident in the substantial mass gain observed for Coatings 1 and 2 during the initial 124 h of the oxidation test. This indicates significant differences in Fe diffusion behavior among the three coatings. In the very early stage of oxidation, Fe diffusivity was influenced by the alloy structure and composition of the coating. The FCC structure found in Fe-Mn-Co-Cu and Fe-Mn-Co-Cu-Ni alloys has denser atomic packing, requiring more energy for vacancy formation and migration, thus typically resulting in slower Fe diffusion compared to the BCC structure of the Fe-Mn-Co alloy at the same temperature. Fig. 9a illustrates the Thermo-calc DICTRA simulation (using TCFE 11 and MOBFE 6 database) of Fe diffusion across the metallic coating/substrate interfaces of the three coated steels under isothermal conditions at 650 °C for 30 min. The simulation results indicate that a substantially higher Fe concentration accumulated in the inner region of Coating 1, whereas Coating 2 and Coating 3 revealed much less Fe diffusion. Furthermore, this interdiffusion behavior is largely influenced by differences in oxygen affinity among the constituent elements. The higher oxygen affinity of Fe likely enhanced its outward diffusion

throughout the coatings. For Coating 3, the minimal Fe diffusion is likely caused by the sluggish diffusion effect, which is a fundamental characteristic of high-entropy materials. Fig. 9b-d presents the predicted volume fraction of oxidation phases for $Fe_x(Mn_{25.0}Co_{37.7})_{1-x}$, $Fe_x(Mn_{22.6}Co_{22.5}Cu_{30.1})_{1-x}$ and $Fe_x(Mn_{16.2}Co_{20.7}Cu_{21.4}Ni_{20.0})_{1-x}$ alloy systems as a function of varying Fe content, simulated by using Thermo-calc simulation (TCOX12 database). The left boundary corresponds to the as-deposited composition of each coating. The dotted region defines the critical compositional window consistent with our experimental observations. Simulation results show increased Fe content in the metallic phase for all three alloy systems, indicating significant elemental diffusion occurring while the coatings remain metallic during early oxidation. For the $Fe_x(Mn_{25}Co_{37.7})_{1-x}$ system, when the Fe/metals ratio in the phase diagram ranges from 0.5 to 0.85, the oxide layer typically consists of spinel ($Fe_{23.24}Co_{14.73}Mn_{2.75}O_{57.28}$–$Fe_{28.71}Co_{14.09}O_{57.20}$), bixbyite ($Mn_{27.08}Fe_{12.70}Co_{0.22}O_{60}$), and hematite ($Fe_{37.26}Mn_{2.7}O_{60}$). This shows strong agreement with the TEM results. On the other hand, in the $Fe_x(Mn_{22.6}Co_{22.5}Cu_{30.1})_{1-x}$ system, an Fe/metals ratio between 0.5 and 0.75 leads to the simultaneous formation of spinel ($Fe_{22.44}Co_{9.02}Cu_{6.86}Mn_{4.44}O_{57.24}$–$Fe_{22.34}Co_{8.01}Cu_{8.01}Mn_{4.40}O_{57.24}$), spinel#2 ($Mn_{19.19}Fe_{11.19}Cu_{10.6}Co_{1.88}O_{57.14}$–$Mn_{18.47}Fe_{11.60}Cu_{11.23}Co_{1.56}O_{57.14}$), and hematite ($Fe_{37.25}Mn_{2.75}O_{60}$–$Fe_{37.52}Mn_{2.48}O_{60}$) in the oxide layer; however, EDS analysis did not detect two distinct spinel compositions, suggesting that the diffusion of additional elements might alter the equilibrium and favor the formation of a single spinel phase for Coating 2. Notably, when the Fe/metals ratio in the $Fe_x(Mn_{16.2}Co_{20.7}Cu_{21.4}Ni_{20.0})_{1-x}$ system is approximately 0.3 to 0.5, the oxide layer exclusively forms a single spinel phase with a composition range of $Fe_{13.91}Mn_{7.24}Co_{7.24}Cu_{7.24}Ni_{7.24}O_{57.14}$–$Fe_{22.47}Mn_{4.56}Co_{5.18}Cu_{5.19}Ni_{5.18}O_{57.41}$. This indicates that despite the unavoidable Fe diffusion into the coating (though less severe in Coating 3), the high-entropy system can provide a sufficiently large single-phase region, thereby preventing the formation of other oxide phases. The volumetric increase observed in Coatings 1 and 2 following oxidation is mainly attributed to the formation of extensive $Fe_2O_3$, which possesses a high Pilling-Bedworth Ratio (PBR $>$ 2.1), leading to significant outward expansion. In contrast, Coating 3 maintains a dense, protective spinel structure and prevents the formation of porous $Fe_2O_3$, thereby minimizing the volumetric expansion of the oxide layer.

As Fe diffused into the coating layers, it left behind defect structures in the surface region of the substrate in steels with Coatings 1 and 2. These defected regions were readily oxidized by the inward diffusion of oxygen, leading to the formation of Cr-Fe mixed oxides. Moreover, The Gibb's formation energy of various oxides at 650 °C, calculated using Materials Thermochemistry [41] and reported by Jian et al. [42], offers a more comprehensive understanding of the positioning of oxide layers. From outermost to innermost, the oxide layers form in an order that follows their formation energy: Cr-lean spinel (first to contact oxygen; similar to $CoFe_2O_4$ at −380 kJ/$mol_{O_2}$ and $CuFe_2O_4$ at −320 kJ/$mol_{O_2}$), followed by $Fe_2O_3$ (−380 kJ/$mol_{O_2}$), then Cr-Fe spinel (e.g., $FeCr_2O_4$ at −565 kJ/$mol_{O_2}$), $(Cr,Fe)_2O_3$, and finally $Cr_2O_3$ (−625 kJ/$mol_{O_2}$). While directly depositing a spinel oxide coating—rather than a metallic layer—might mitigate Fe diffusion, it presents significant challenges regarding residual stress and interfacial adhesion [43,44]. In contrast, the two-step fabrication process employed in this study (metallic deposition followed by thermal oxidation) promotes elemental inter-diffusion at the coating-substrate interface, as evidenced by the excellent adhesion of the (Fe,Mn,Co,Cu,Ni)-spinel and other spinel coatings reported previously [24–28]. This mechanism significantly enhances interfacial bonding, thereby ensuring the structural integrity of the spinel scale during high-temperature service. Overall, the significant mass gain observed in Coatings 1 and 2 compared to Coating 3 reflects the anomalous growth of hematite and (Cr, Fe)-oxide structures. These structures prematurely compromise long-term durability regarding Cr-evaporation resistance and ASR performance, as discussed in the following sections.

### 4.2. Superior electrical performance of quinary multi-component spinel oxide coating

While the uncoated SUS430 initially exhibits a lower ASR than that of the coated samples, this initial advantage diminishes rapidly over time. As shown in Supplementary Figure S1, the increase in the ASR of the uncoated substrate is attributed to the continuous thickening of the resistive $Cr_2O_3$-rich scale. From the perspective of long-term stability, a protective coating is essential to suppress this excessive scale growth. Notably, the ASR of Coating 3 became lower than that of the uncoated substrate after 500 h, demonstrating its long-term durability. The significant differences in ASR performance among the three coatings are likely due to the presence and the thickness of hematite layers and Cr-Fe oxide structures. As reported by Tomas et al. [22], the thermally sprayed Mn-Co-coated SUS441, exhibiting a homogeneous microstructure (10 μm in thickness) and an thin chromia layer (200 nm in thickness) after oxidation, showed an ASR value of approximately 10 mΩ·cm$^2$ at 650 °C. In contrast, the thermally sprayed Cu-coated SUS441 and Mn-Cu-coated SUS441, prepared under the same processing parameters and both containing abnormal Fe-rich oxide layer and Cr-Fe oxide structures after oxidation, exhibited significantly higher ASR values of ~52 mΩ·cm$^2$ and 19 mΩ·cm$^2$, respectively [22]. These results confirm the detrimental effects of hematite layer and Cr-Fe oxides on the ASR values, consistent with observations in Coating 1 and Coating 2 coated steels. On the other hand, the ASR value of 524-hour oxidized Coating 3-coated steel (8.8 mΩ·cm$^2$) is even lower than that of Mn-Co-coated SUS441 (~10 mΩ·cm$^2$) [22] and $Mn_{1.35}Co_{1.35}Cu_{0.2}Y_{0.1}O_4$-coated SUS441 (~11 mΩ·cm$^2$) [45] under the same testing temperature. According to the following Equation, the ASR value of a sample can be roughly estimated:

$$ASR = A{\cdot}R = \Sigma(\rho_i l_i) \tag{3}$$

where $\rho_i$(Ω·cm) and $l_i$(cm) represent the electrical resistivity (specific resistance) and thickness of different type of oxide layer, respectively. And Table 3 presents the thickness, electrical resistivity of each oxide structure [46–48], theoretically calculated ASR values and the experimentally obtained ASR values for all samples after 524 h of oxidation test. The oxide scales formed on the coated steels after 524-hour oxidation test were characterized by distinct layers of $Cr_2O_3$, $(Cr,Fe)_2O_3$, $(Cr,Fe)_3O_4$, hematite ($Fe_2O_3$), and Cr-lean spinel. And the bixbyite phase in Coating 1 was assumed to be dispersed within the spinel layer and have a negligible effect on the ASR. The electrical resistivity of $(Cr,Fe)_2O_3$ is calculated based on the proportion of $Cr_2O_3$ and $Fe_2O_3$. Since the oxide layer thickness and composition varied significantly across the thick and thin regions of Coating 1 and Coating 2, theoretical ASR values were calculated separately for each region. Given the easier electrical conduction of the thinner section, the total contribution of the thick and thin regions (except for spinel layers) follows a parallel equivalent circuit model, where the fractions of these regions are considered equal:

$$\frac{1}{ASR_{Excluding\ spinel\ layer}} = \frac{0.5}{ASR_{Thick\ region}} + \frac{0.5}{ASR_{Thin\ region}} \tag{4}$$

Accordingly, the calculated theoretical ASR value for Coating 1 is 19.08 mΩ·cm$^2$. Therefore, the electrical resistivity of $Fe_{26.3}Co_{14.5}Mn_{6.7}Cr_{4.5}O_{48.2}$ spinel was determined to be approximately 13.7 Ω·cm by subtracting the theoretical ASR value (19.08 mΩ·cm$^2$) from the experimental ASR value and dividing by the spinel thickness. Following the same method, the electrical resistivity for both $Fe_{23.6}Cu_{9.0}Mn_{7.0}Co_{5.5}Cr_{0.45}O_{54.5}$ spinel and $Fe_{15.9}Cu_{8.7}Mn_{8.8}Co_{7.8}Ni_{3.1}Cr_{1.9}O_{53.5}$ spinel is approximately 3 Ω·cm. Compositionally, the incorporation of Cu into spinel structure effectively reduced the resistivity of the Fe-Mn-Co-based spinel. It has been well established that Cu possesses two valence states ($Cu^+/Cu^{2+}$) at octahedral sites in spinel lattice, and it can facilitate the oxidation of $Mn^{3+}$ to $Mn^{4+}$ [24,45]. However, our XPS findings reveal that the incorporation of Cu does not simply increase the

$Mn^{4+}$ fraction. Instead, the increase in $Mn^{2+}$ suggests a higher tendency for these ions to occupy tetrahedral sites [49]. This redistribution could effectively shift the $Mn^{4+}/Mn^{3+}$ ratio toward an ideal value of ~1 within the octahedral sites. Furthermore, the addition of Cu and Ni facilitates a more balanced $Co^{3+}/ Co^{2+}$ ratio compared to Coating 1. These phenomena promote polaron hopping between the cations at octahedral sites (forming mixed-valence exchange pairs) [50], which likely accounts for the increasing electrical conductivity. A similar approach was employed to compare the resistivity of spinels in previously reported coated samples (FeCoNi [28], NiFe [27], and CuFe [26] coatings). These samples were typically oxidized at 800 °C before ASR testing at 650 °C. Considering the influence of grain growth, a $Cr_2O_3$ resistivity of 116 Ω·cm was chosen for calculation, as it best matches the ASR results reported in the literature [51]. Based on this, the calculated resistivities at 650 °C for $(Fe,Co,Ni)_3O_4$, $NiFe_2O_4$, and $CuFe_2O_4$ are approximately 10–12 Ω·cm, 90–100 Ω·cm, and 92 Ω·cm, respectively. Notably, these values are 1–2 order of magnitude larger than their respective bulk values ($CoFe_2O_4$: 1.675 Ω·cm [52], $NiFe_2O_4$: 18.52 Ω·cm [52], $CuFe_2O_4$: 0.22 Ω·cm [52]). This discrepancy is likely attributed to microstructural factors such as grain size, porosity, and other defect structures within the oxide layer. In summary, a comparison of the microstructure and composition effects on ASR values across the three coated steels in this work reveals that high-entropy systems not only mitigate the detrimental effects of hematite and Cr-Fe oxides on ASR, as observed in Coating 1 and Coating 2 coated steels, but also contribute to an improvement in the conductivity of the spinel phase itself.

### 4.3. The suppression of Cr evaporation

Cr evaporation from stainless steel is primarily attributed to the formation of volatile $CrO_2(OH)_2$ and $CrO_3$ species from $Cr_2O_3$ scale [19,53]. This evaporation process is typically diffusion-controlled at 650 °C, depending on the diffusivity of Cr and the ability of the oxide layers to dissolve or retain Cr. For the uncoated SUS430, this behavior is suppressed by the formation of an $(Mn,Cr)_3O_4$ scale on top of $Cr_2O_3$, as Cr exhibits lower activity within its structure [54,55]. However, the limited growth of $(Mn,Cr)_3O_4$ caused by the lower Mn content restricts its protective ability. This is evidenced by Cr evaporation 6–10 times higher than those of the coated steels, contributing to the relatively lower mass gain observed due to the significant loss of volatile species. Notably, the Cr evaporation rate of Coating 3-coated SUS430 was reduced by approximately one order of magnitude, making it comparable to that of a 600 nm Co/Cu/MnCu coating with a Ce diffusion barrier [22].

It is worth noting that no spallation or delamination was observed in any of the three coatings after the oxidation and Cr-evaporation tests. Therefore, the differences in Cr-evaporation resistance are primarily attributed to the structural (e.g., phase, porosity) and compositional characteristics of the coatings. For Coating 1 and Coating 2 coated steels, although the Cr-Fe oxides and hematite layers can impede Cr outdiffusion through a diffusion-controlled mechanism, their high porosity (along with that of the spinel layers)—as demonstrated by the cross-sectional SEM morphologies (Figs. 2 and 3) and TEM analysis (Fig. 5)—likely creates short-circuit diffusion paths for Cr, consequently resulting in a significant decrease in Cr-evaporation resistance. In contrast, the quinary multi-component spinel layer of Coating 3 coated steel led to a stable and compact oxide layer microstructure. Consequently, Coating 3 demonstrated superior Cr diffusion resistance and oxidation resistance compared to the other two coatings.

## 5. Conclusion

In this study, three alloy coatings—Fe-Mn-Co (Coating 1), Fe-Mn-Co-Cu (Coating 2), and Fe-Mn-Co-Cu-Ni (Coating 3)—were deposited on SUS430 ferritic stainless steel and oxidized at 650 °C to evaluate their suitability as protective spinel-based coatings for SOFC interconnects. The key results are summarized as follows:

1. Characterization using EDS, EBSD, TEM, and XRD analysis indicated that at 650 °C, the oxide scales formed on Coating 1 and Coating 2 coated steels consisted of a multiphase structure comprising an innermost chromia-rich oxide layer, Cr-Fe oxide structures (a mixture of corundum and spinel phases), a hematite layer, and an outermost spinel layer. In contrast, an inner chromia layer and outer quinary multi-component spinel layer were identified on Coating 3 coated steel.
2. The observed variations in oxide layer structure are determined by the Fe content diffusing from the substate into the coating during oxidation. While Cu or Cu-Ni addition can reduce Fe diffusion by promoting a BCC to FCC transformation of the coatings, the sluggish diffusion effect resulting from the quinary composition of Coating 3 plays a more crucial role in inhibiting the formation of hematite and Cr-Fe oxides.
3. The quinary composition of Coating 3 mitigated the detrimental effects of hematite and Cr-Fe oxides on ASR. Furthermore, the incorporation of Cu into the spinel structure effectively improved the electrical conductivity of Fe-Mn-Co-based spinel.
4. The quinary composition of Coating 3 is beneficial for stabilizing the composition of the coating elements and expanding the compositional range for single-phase spinel. These factors lead to improved thermal stability and Cr-evaporation resistance.
5. The results highlight the effectiveness of high-entropy compositional design in tuning oxide phase stability, suppressing deleterious oxide formation, and enhancing both electrical and oxidation performance. Such coatings offer a promising pathway for improving the long-term stability and efficiency of SOFC interconnects at 650 °C.

## Declaration of generative AI and AI-assisted technologies in the manuscript preparation process

During the preparation of this work, the authors used Gemini (Google) to improve the clarity and grammar of the English text. After using these tools, the authors reviewed and edited the content as needed and take full responsibility for the content of the published article.

## CRediT authorship contribution statement

**Cheng-Ju Tsai:** Writing – original draft, Visualization, Validation, Methodology, Investigation, Formal analysis, Data curation, Conceptualization. **Hideyuki Murakami:** Writing – review & editing, Methodology. **Yoshiaki Toda:** Writing – review & editing. **Fan-Yi Ouyang:** Writing – review & editing, Resources. **Hyoung Seop Kim:** Writing – review & editing, Supervision. **An-Chou Yeh:** Writing – review & editing, Writing – original draft, Visualization, Supervision, Software, Resources, Project administration, Methodology, Investigation, Funding acquisition, Formal analysis, Conceptualization.

## Declaration of competing interest

The authors declare that they have no known competing financial interests or personal relationships that could have appeared to influence the work reported in this paper.

## Acknowledgement

This work was financially supported by the “High Entropy Materials Center” from The Featured Areas Research Center Program within the framework of the Higher Education Sprout Project by the Ministry of Education (MOE) in Taiwan. This work was also supported by National Science and Technology Council (NSTC) in Taiwan under Grant NSTC 114-2221-E-007-085-MY3.

## Supplementary materials

Supplementary material associated with this article can be found, in the online version, at doi:10.1016/j.apsadv.2026.100956.

## Data availability

Data will be made available on request.

## References


[1] IEA, World Energy Outlook 2023, International Energy Agency, Paris, France, 2023 [Online]. Available, https://www.iea.org/reports/world-energy-outlook-2023.

[2] L. Li, et al., Review and outlook on the international renewable energy development, Energy Built Environ. 3 (2) (2022) 139–157, https://doi.org/10.1016/j.enbenv.2020.12.002.

[3] M.L. Perry, T.F. Fuller, A historical perspective of fuel cell technology in the 20th century, J. Electrochem. Soc. 149 (7) (2002) S59–S67, https://doi.org/10.1149/1.1488651. Review vol.

[4] Z. Salameh, Chapter 4 - energy storage, in: Z. Salameh (Ed.), Renewable Energy System Design, Academic Press, Boston, 2014, pp. 201–298.

[5] M. Singh, D. Zappa, E. Comini, Solid oxide fuel cell: decade of progress, future perspectives and challenges, Int. J. Hydrog. Energy 46 (54) (2021) 27643–27674, https://doi.org/10.1016/j.ijhydene.2021.06.020.

[6] S. Mekhilef, R. Saidur, A. Safari, Comparative study of different fuel cell technologies, Renew. Sustain. Energy Rev. 16 (1) (2012) 981–989, https://doi.org/10.1016/j.rser.2011.09.020.

[7] T.S. Zhang, J. Ma, H. Cheng, S.H. Chan, Ionic conductivity of high-purity Gd-doped ceria solid solutions, Mater. Res. Bull. 41 (3) (2006) 563–568, https://doi.org/10.1016/j.materresbull.2005.09.008.

[8] D.J. Seo, K.O. Ryu, S.B. Park, K.Y. Kim, R.-H. Song, Synthesis and properties of Ce1−xGdxO2−x/2 solid solution prepared by flame spray pyrolysis, Mater. Res. Bull. 41 (2) (2006) 359–366, https://doi.org/10.1016/j.materresbull.2005.08.012.

[9] A. Kirubakaran, S. Jain, R.K. Nema, A review on fuel cell technologies and power electronic interface, Renew. Sustain. Energy Rev. 13 (9) (2009) 2430–2440, https://doi.org/10.1016/j.rser.2009.04.004.

[10] J. Wu, X. Liu, Recent development of SOFC metallic interconnect, J. Mater. Sci. Technol. 26 (4) (2010) 293–305, https://doi.org/10.1016/S1005-0302(10)60049-7.

[11] T. Jin, K. Lu, Chemical compatibility between Sr-doped lanthanum manganite air electrode and AISI 441 interconnect, Int. J. Hydrog. Energy 36 (7) (2011) 4440–4448, https://doi.org/10.1016/j.ijhydene.2011.01.013.

[12] Z.G. Yang et al., "Investigation of AISI 441 ferritic stainless steel and development of spinel coatings for SOFC interconnect applications," 2008, doi: 10.2172/1019232.

[13] J.H. Zhu, D.A. Chesson, Y.T. Yu, Review—(Mn,Co)3O4-based spinels for SOFC interconnect coating application, J. Electrochem. Soc. 168 (11) (2021) 114519, https://doi.org/10.1149/1945-7111/ac3a29.

[14] A. Petric, H. Ling, Electrical conductivity and thermal expansion of spinels at elevated temperatures, J. Am. Ceram. Soc. 90 (5) (2007) 1515–1520, https://doi.org/10.1111/j.1551-2916.2007.01522.x.

[15] L. Gan, H. Murakami, I. Saeki, High temperature oxidation of Co-W electroplated type 430 stainless steel for the interconnect of solid oxide fuel cells, Corros. Sci. 134 (2018) 162–168, https://doi.org/10.1016/j.corsci.2018.02.026.

[16] L. Gan, T. Yamamoto, H. Murakami, Microstructure and diffusion behavior in the multilayered oxides formed on a Co–W electroplated ferritic stainless steel followed by oxidation treatment, Acta Mater. 194 (2020) 295–304, https://doi.org/10.1016/j.actamat.2020.04.048.

[17] L. Gan, T. Nishimura, S.A. Sheikh, I. Saeki, H. Murakami, Thermal stability of the CoWO4 layer formed on ferritic stainless steel, Corros. Sci. 176 (2020) 109037, https://doi.org/10.1016/j.corsci.2020.109037.

[18] L. Gan, X. Montero, S.A. Sheikh, I. Saeki, H. Murakami, Microstructure and area specific resistance of cathodic half cells for solid oxide fuel cells composed of perovskite-type cathodes and Co-alloy-coated ferritic stainless steel interconnects, Surf. Coat. Technol. 406 (2021) 126659, https://doi.org/10.1016/j.surfcoat.2020.126659.

[19] R. Spotorno, D. Paravidino, S. Delsante, P. Piccardo, Volatilization of chromium from AISI 441 stainless steel: time and temperature dependence, Surf. Coat. Technol. 433 (2022) 128125, https://doi.org/10.1016/j.surfcoat.2022.128125.

[20] M.J. Reddy, J.-E. Svensson, J. Froitzheim, Evaluating candidate materials for balance of plant components in SOFC: oxidation and Cr evaporation properties, Corros. Sci. 190 (2021) 109671, https://doi.org/10.1016/j.corsci.2021.109671.

[21] H. Falk-Windisch, J. Claquesin, M. Sattari, J.-E. Svensson, J. Froitzheim, Co- and Ce/Co-coated ferritic stainless steel as interconnect material for intermediate temperature solid oxide fuel cells, J. Power Sources 343 (2017) 1–10, https://doi.org/10.1016/j.jpowsour.2017.01.045.

[22] M. Tomas, V. Asokan, J. Puranen, J.E. Svensson, J. Froitzheim, Efficiencies of cobalt- and copper-based coatings applied by different deposition processes for applications in intermediate-temperature solid oxide fuel cells, Int. J. Hydrog. Energy 47 (76) (2022) 32628–32640, https://doi.org/10.1016/j.ijhydene.2022.07.168.

[23] C.M. Rost, et al., Entropy-stabilized oxides, Nat. Commun. 6 (1) (2015) 8485, https://doi.org/10.1038/ncomms9485.

[24] Q. Zhao, S. Geng, Y. Zhang, G. Chen, S. Zhu, F. Wang, High-entropy FeCoNiMnCu alloy coating on ferritic stainless steel for solid oxide fuel cell interconnects, J. Alloys Compd. 908 (2022) 164608, https://doi.org/10.1016/j.jallcom.2022.164608.

[25] S. Geng, et al., Sputtered MnCu metallic coating on ferritic stainless steel for solid oxide fuel cell interconnects application, Int. J. Hydrog. Energy 42 (15) (2017) 10298–10307, https://doi.org/10.1016/j.ijhydene.2017.01.178.

[26] Y. Pan, S. Geng, G. Chen, F. Wang, CuFe2O4/CuO coating for solid oxide fuel cell steel interconnects, Int. J. Hydrog. Energy 46 (44) (2021) 22942–22955, https://doi.org/10.1016/j.ijhydene.2021.04.117.

[27] Q. Zhao, S. Geng, G. Chen, F. Wang, Application of sputtered NiFe2 alloy coating for SOFC interconnect steel, J. Alloys Compd. 769 (2018) 120–129, https://doi.org/10.1016/j.jallcom.2018.07.333.

[28] M. Zhao, S. Geng, G. Chen, F. Wang, FeCoNi converting coating for solid oxide fuel cell steel interconnect application, J. Power Sources 414 (2019) 530–539, https://doi.org/10.1016/j.jpowsour.2019.01.045.

[29] R. Schmidt, A. Basu, A.W. Brinkman, Small polaron hopping in spinel manganates, Phys. Rev. B 72 (11) (2005) 115101, https://doi.org/10.1103/PhysRevB.72.115101.

[30] B. Cantor, I.T.H. Chang, P. Knight, A.J.B. Vincent, Microstructural development in equiatomic multicomponent alloys, Mater. Sci. Eng.: A 375-377 (2004) 213–218, https://doi.org/10.1016/j.msea.2003.10.257.

[31] Properties and selection—Irons, steels, and high-performance alloys, in: Metals Handbook, 1, ASM International, Materials Park, OH, 1990. https://www.matweb.com (accessed Oct. 11, 2025, data accessed via MatWeb).

[32] T.K. van Leeuwen, Condensation of Chromium Vapor, Generated In High-Temperature (>800 °C) Environments, and Interactions with Aluminosilicate Surfaces, Montana State University, Bozeman, 2024.

[33] M. Bertoldi, et al., Protective coatings of metallic interconnects for IT-SOFC application, J. Fuel. Cell Sci. Technol. 5 (1) (2008) 11001, https://doi.org/10.1115/1.2713761.

[34] N. Laegreid, G.K. Wehner, Sputtering yields of metals for Ar+ and Ne+ ions with energies from 50 to 600 ev, J. Appl. Phys. 32 (3) (1961) 365–369, https://doi.org/10.1063/1.1736012.

[35] C. Sha, Z. Zhou, Z. Xie, P. Munroe, FeMnNiCoCr-based high entropy alloy coatings: effect of nitrogen additions on microstructural development, mechanical properties and tribological performance, Appl. Surf. Sci. 507 (2020) 145101, https://doi.org/10.1016/j.apsusc.2019.145101.

[36] J. Mao, et al., Initial stage oxidation corrosion of commercial ferritic stainless steels with different Cr contents at 650 °C for solid oxide fuel cells, Heliyon 10 (12) (2024), https://doi.org/10.1016/j.heliyon.2024.e33245.

[37] T. Yamashita, P. Hayes, Analysis of XPS spectra of Fe2+ and Fe3+ ions in oxide materials, Appl. Surf. Sci. 254 (8) (2008) 2441–2449, https://doi.org/10.1016/j.apsusc.2007.09.063.

[38] O.A. Bulavchenko, et al., In situ study of reduction of MnxCo3–xO4 mixed oxides: the role of Manganese content, Inorg. Chem. 60 (21) (2021) 16518–16528, https://doi.org/10.1021/acs.inorgchem.1c02379.

[39] J. Gao, et al., Entropy-engineered Ni–Mn–Co spinel coatings via microwave sintering for ultra-stable SOFC interconnects, Int. J .Hydrog. Energy 170 (2025) 151198, https://doi.org/10.1016/j.ijhydene.2025.151198.

[40] C.V. Ramana, M. Massot, C.M. Julien, XPS and raman spectroscopic characterization of LiMn2O4 spinels, Surf. Interface Anal. 37 (4) (2005) 412–416, https://doi.org/10.1002/sia.2022.

[41] J.V. Wood, Materials thermochemistry, Surf. Eng. 9 (4) (1993) 277–278, https://doi.org/10.1179/sur.1993.9.4.277.

[42] P. Jian, L. Jian, H. Bing, G. Xie, Oxidation kinetics and phase evolution of a Fe–16Cr alloy in simulated SOFC cathode atmosphere, J. Power Sources 158 (1) (2006) 354–360, https://doi.org/10.1016/j.jpowsour.2005.09.056.

[43] S. Molin, et al., Microstructural and electrical characterization of Mn-Co spinel protective coatings for solid oxide cell interconnects, J. Eur. Ceram. Soc. 37 (15) (2017) 4781–4791, https://doi.org/10.1016/j.jeurceramsoc.2017.07.011.

[44] V.I. Gorokhovsky, et al., Deposition and evaluation of protective PVD coatings on ferritic stainless steel SOFC interconnects, J. Electrochem. Soc. 153 (10) (2006) A1886, https://doi.org/10.1149/1.2266244.

[45] I. Thaheem, D.W. Joh, T. Noh, K.T. Lee, Highly conductive and stable Mn1.35Co1.35Cu0.2Y0.1O4 spinel protective coating on commercial ferritic stainless steels for intermediate-temperature solid oxide fuel cell interconnect applications, Int. J. Hydrog. Energy 44 (8) (2019) 4293–4303, https://doi.org/10.1016/j.ijhydene.2018.12.173.

[46] J.H. Park, K. Natesan, Electronic transport in thermally grown Cr2O3, Oxid. Met. 33 (1) (1990) 31–54, https://doi.org/10.1007/BF00665668.

[47] B. Gillot, F. Jemmali, A. Rousset, Kinetics and mechanism of ferrous spinel oxidation studied by electrical conductivity and thermogravimetry, J. Mater. Sci. 21 (12) (1986) 4436–4442, https://doi.org/10.1007/BF01106568.

[48] R.F.G. Gardner, F. Sweett, D.W. Tanner, The electrical properties of alpha ferric oxide—I.: the impure oxide, J. Phys. Chem. Solids 24 (10) (1963) 1175–1181, https://doi.org/10.1016/0022-3697(63)90234-8.

[49] V.S. Urusov, Interaction of cations on octahedral and tetrahedral sites in simple spinels, Phys. Chem. Min. 9 (1) (1983) 1–5, https://doi.org/10.1007/BF00309461.

[50] Y. Liu, J.W. Fergus, C.D. Cruz, Electrical properties, cation distributions, and thermal expansion of manganese cobalt chromite spinel oxides, J. Am. Ceram. Soc. 96 (6) (2013) 1841–1846, https://doi.org/10.1111/jace.12254.

[51] A. Holt, P. Kofstad, Electrical conductivity and defect structure of Cr2O3. II. Reduced temperatures (<~1000 °C), Solid State Ion. 69 (2) (1994) 137–143, https://doi.org/10.1016/0167-2738(94)90402-2.

[52] H. Ling, A. Petric, Electrical and thermal properties of spinels, in: Proc. Vol. 2005-07, 2005, pp. 1866–1873, https://doi.org/10.1149/200507.1866PV.
[53] D.D.K. Hilpert, M. Miller, D.H. Peck, R. Weiß, Chromium vapor species over solid oxide fuel cell interconnect materials and their potential for degradation processes, J. Electrochem. Soc. 143 (1996) 3642–3647, https://doi.org/10.1149/1.1837264.
[54] G.R. Holcomb, D.E. Alman, The effect of manganese additions on the reactive evaporation of chromium in Ni–Cr alloys, Scr. Mater. 54 (10) (2006) 1821–1825, https://doi.org/10.1016/j.scriptamat.2006.01.026.
[55] G.R. Holcomb, Calculation of reactive-evaporation rates of chromia, Oxid. Met. 69 (3) (2008) 163–180, https://doi.org/10.1007/s11085-008-9091-4.